

Pyrrolo[1,2-*a*]quinoxalines: Insulin Mimetics that Exhibit Potent and Selective Inhibition against Protein Tyrosine Phosphatase 1B

Javier García-Marín,^[a, b, f] Mercedes Griera,^[b, c] Patricia Sánchez-Alonso,^[a] Bruno Di Geronimo,^[d] Francisco Mendicuti,^[e, f] Manuel Rodríguez-Puyol,^{*,[b, c]} Ramón Alajarín,^{*,[a, b, f]} Beatriz de Pascual-Teresa,^[d] Juan J. Vaquero,^{*,[a, b, f]} and Diego Rodríguez-Puyol^{*,[b, c]}

PTP1B dephosphorylates insulin receptor and substrates to modulate glucose metabolism. This enzyme is a validated therapeutic target for type 2 diabetes, but no current drug candidates have completed clinical trials. Pyrrolo[1,2-*a*]quinoxalines substituted at positions C1–C4 and/or C7–C8 were found to be nontoxic to cells and good inhibitors in the low- to sub-micromolar range, with the 4-benzyl derivative being the most potent inhibitor (0.24 μM). Some analogues bearing chlorine atoms at C7 and/or C8 kept potency and showed good selectivity compared to TCPTP (selectivity index > 40). The most

potent inhibitors behaved as insulin mimetics by increasing glucose uptake. The 4-benzyl derivative inhibited insulin receptor substrate 1 and AKT phosphorylation. Molecular docking and molecular dynamics simulations supported a putative binding mode for these compounds to the allosteric $\alpha 3/\alpha 6/\alpha 7$ pocket, but inconsistent results in enzyme inhibition kinetics were obtained due to the high tendency of these inhibitors to form stable aggregates. Computational calculations supported the druggability of inhibitors.

Introduction

Protein tyrosine phosphatase 1B (PTP1B) dephosphorylates insulin receptor (IR) and substrates (IRS), thereby modulating glucose metabolism.^[1,2] In addition, it is a validated therapeutic target for type 2 diabetes mellitus (T2DM) as PTP1B knockout mice and tissue-specific deletion of this enzyme lead to better

insulin sensitivity and glucose tolerance.^[3–5] Furthermore, PTP1B-targeting antisense nucleotides have been shown to exhibit anti-diabetic effects.^[6,7]

The search for PTP1B inhibition-based anti-diabetes drug candidates is still an unresolved issue despite almost two decades of both industrial and academic research. Although many different inhibitors have been reported (Figure 1), PTP1B has remained an elusive target for many years. Currently, there

[a] J. García-Marín, Dr. P. Sánchez-Alonso, Dr. R. Alajarín, Prof. J. J. Vaquero
Departamento de Química Orgánica y Química Inorgánica
Universidad de Alcalá

28805 Alcalá de Henares (Spain)

E-mail: ramon.alajarin@uah.es

juanjose.vaquero@uah.es

[b] J. García-Marín, M. Griera, Prof. M. Rodríguez-Puyol, Dr. R. Alajarín,
Prof. J. J. Vaquero, Dr. D. Rodríguez-Puyol

Instituto Ramón y Cajal de Investigación Sanitaria (IRYCIS)

Ctra. Colmenar Viejo, km. 9100

28034 Madrid (Spain)

E-mail: manuel.rodriguez@uah.es

diego.rodriguez@uah.es

[c] M. Griera, Prof. M. Rodríguez-Puyol, Dr. D. Rodríguez-Puyol

Departamento de Biología de Sistemas

Universidad de Alcalá

28805 Alcalá de Henares (Spain)

[d] B. Di Geronimo, Prof. B. de Pascual-Teresa

Departamento de Química y Bioquímica

Facultad de Farmacia, Universidad San Pablo CEU

28925 Alcorcón (Spain)

[e] Prof. F. Mendicuti

Departamento de Química Analítica, Química Física e Ingeniería Química

Universidad de Alcalá

28805 Alcalá de Henares (Spain)

[f] J. García-Marín, Prof. F. Mendicuti, Dr. R. Alajarín, Prof. J. J. Vaquero

Instituto de Investigación Química Andrés M. del Río

Facultad de Farmacia, Universidad de Alcalá

28805 Alcalá de Henares (Spain)



Supporting information for this article is available on the WWW under
<https://doi.org/10.1002/cmdc.202000446>

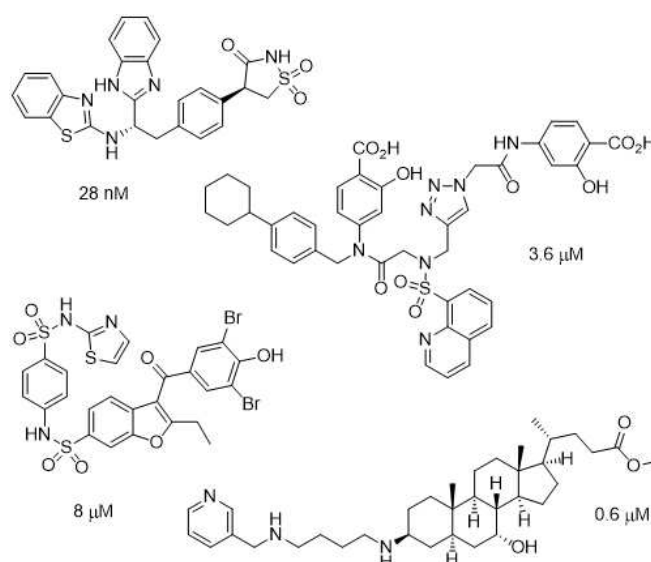


Figure 1. Representative examples of PTP1B inhibitors and their IC_{50} data: pTyr mimetic (top left) and bidentate (top right) catalytic-site inhibitors, allosteric inhibitors at the $\alpha 3/\alpha 6/\alpha 7$ site (bottom left) and at the disordered C-terminal site (bottom right).

is no drug-like PTP1B inhibitor in post-phase II clinical trials.^[8–11] Since the discovery of the first PTP1B inhibitor,^[12] many potent competitive phosphotyrosine (pTyr)-mimetic PTP1B inhibitors have been reported.^[13,14] However, these ligands normally show low selectivity due to the highly conserved catalytic site in the phosphatase superfamily. They also frequently show poor oral bioavailability since they need to be negatively charged in order to bind the highly positively charged catalytic pocket. Although druggability of phosphatases has been a controversial issue,^[15,16] the allosteric site of PTP1B exhibits better druggability than the catalytic pocket.^[17]

Binding sites other than the catalytic pocket (site A) have been reported. Thus, in addition to the active site and its immediate surroundings,^[18] there are several binding pockets (sites B, C, D and E) with two of them reported as secondary pTyr binding pockets.^[19–21] Somewhat farther from the catalytic pocket, there is an allosteric binding pocket surrounded by $\alpha 3$, $\alpha 6$ and $\alpha 7$ helices,^[22] and a further allosteric site has been reported in the disordered C-terminal non-catalytic segment.^[23]

During a biological screening of in-house compound libraries, 4-methylpyrrolo[1,2-*a*]quinoxaline (**1a**) was found to be a hit for PTP1B inhibition (Figure 2). As such, we started a hit-to-lead program based on this scaffold that involved synthesizing a series of pyrrolo[1,2-*a*]quinoxalines **1** bearing substituents at the benzene (Domain 1) and pyrrole (Domain 2) rings and at R⁴ (Domain 3), as depicted in Figure 2. We also performed the *in vitro* inhibition of PTP1B, enzyme kinetics assays, spectroscopic measurements for aggregate formation, cell experiments for glucose uptake and PTP1B-substrates (IRS1, AKT, STAT3) phosphorylation, as well as molecular docking and molecular dynamics. In this article we report the identification of a new class of PTP1B inhibitors based on this pyrrolo[1,2-*a*]quinoxaline scaffold.

Results and Discussion

Chemistry

The synthesis of pyrrolo[1,2-*a*]quinoxalines has recently attracted renewed interest due to the biological activities shown by compounds based on this scaffold.^[24] We followed a classical approach by using commercially available ortho-nitroanilines **2** as building blocks to provide the substituents at Domain 1. Carboxylic acid anhydrides or chlorides, or methyl orthoformate, allowed diversification at Domain 3, whereas *N*-bromosuccinimide was the bromine source at Domain 2 (Figure 2).

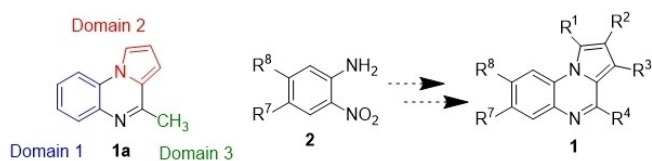
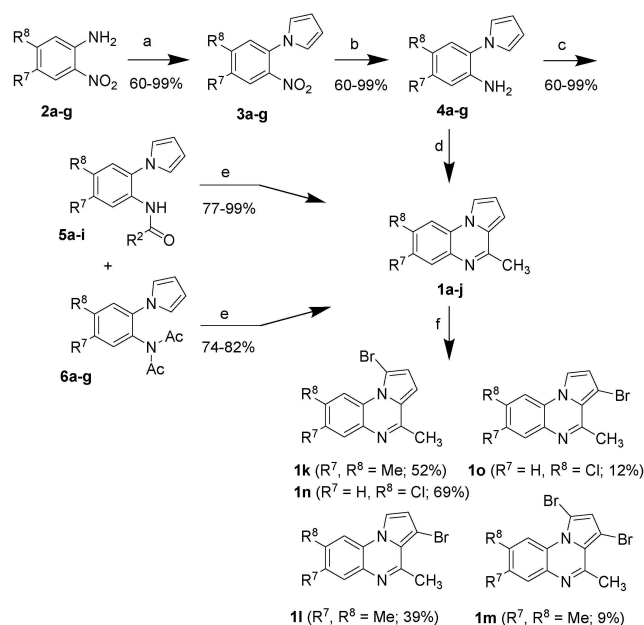


Figure 2. Hit compound **1a** with domains to explore and synthetic design for compounds **1**.

Compounds **1** were prepared using the classical method involving POCl₃-mediated cyclization of *N*-(2-acylamino-phenyl) pyrroles (Scheme 1).^[25]

The pyrrole ring was constructed initially using a Clauson-Kaas synthesis with commercially available 2-nitroanilines **2** to give 1*H*-1-(2-nitrophenyl)pyrroles **3** (60–99%). Compound **3e** was obtained in the lowest yield due to formation of the corresponding indole derivative (10%) as a by-product. Compounds **3** were then reduced to anilines **4** (52–91%) by catalytic hydrogen-transfer reaction using hydrazine and Pd on carbon or by reduction with SnCl₂. Hydrazine only worked well with **3a** (91%), whereas the reaction with **3b** was incomplete and yielded the intermediate azoxy compound, as detected by HPLC-MS analysis of the reaction mixture. Reduction of the nitro group in **3b–j** was performed with SnCl₂. Anilines **4** were acetylated with Ac₂O or an acyl chloride to give amides **5** (70–93%) together with small amounts of imides **6** (5–15%) as by-product. Cyclisation of **5** in refluxing POCl₃ led to **1a–i** (77–91%). Heating **6** for a longer reaction time also yielded **1a–i** (74–82%). For **1j**, treatment of **4a** with methyl orthoformate resulted in acylation and cyclisation in a single step. The substitution pattern at the pyrrole ring was explored by bromination of **1b** and **1g** with NBS, which yielded mixtures of mono- and dibromo derivatives **1k–m** and **1n,o**, respectively. Compound **1b** gave a mixture of **1k** (52%), **1l** (39%) and **1m** (8%), whereas **1g** provided a mixture of **1n** (69%) and **1o** (12%). Structural determination of the bromo derivatives was based on chemical shifts and coupling constants reported for the pyrrolo[1,2-*a*]quinoxaline core,^[26] as well as nuclear Overhauser effect (NOE) and HMBC experiments. Compounds **1k**,



Scheme 1. Synthesis of pyrrolo[1,2-*a*]quinoxalines **1**. a) 2,5-dimethoxytetrahydrofuran, AcOH, reflux; b) SnCl₂·2H₂O, EtOH, reflux; or N₂H₄, 10% Pd/C, EtOH (for **3a**); c) Ac₂O, AcOH, reflux; or ROCOCl, Et₃N, CH₂Cl₂ (for **1h** and **1i**); d) HC(OMe)₃, cat. AcOH, reflux (for **1j**); e) POCl₃, reflux; f) NBS, DMF, –10 °C to room temp.

1 m and **1 n** showed a NOE between H3 and CH₃ at C4, whereas **1 l** and **1 o** showed a NOE between H1 and H9.

PTP1B/ TCPTP in vitro inhibitory activity and selectivity

Compounds **1** were screened using single substrate and inhibitor concentrations (Figure 3), with the colorimetric malachite green assay being used as method of choice. Assays were carried out using human recombinant PTP1B (residues 1–322; 37.4 kDa; 2.5 ng), inhibitor (1 μM) and insulin receptor substrate 5 (IRS-5, 75 μM, *k_m* = 85 μM), a phosphopeptide containing residue sequence 1142–1153 and the pTyr1146 residue from the insulin receptor (IR) β-subunit domain. The compounds tested showed inhibitory activity of between 22 and 53% inhibition at 1 μM.

Compounds **1 h–j** were prepared after the activity screening was performed and were later assayed for inhibitor activity. The inhibitor concentration at 50% inhibition (*IC*₅₀) was assayed for compounds **1** using human recombinant PTP1B (residues 1–322; MW = 37.4 kDa; 1.6 nM), *para*-nitrophenyl phosphate (pNPP, *k_m* = 0.38 mM) and five inhibitor concentrations between 0.04 and 25 μM.^[27] The best inhibitors **1 d, g–j** exhibited

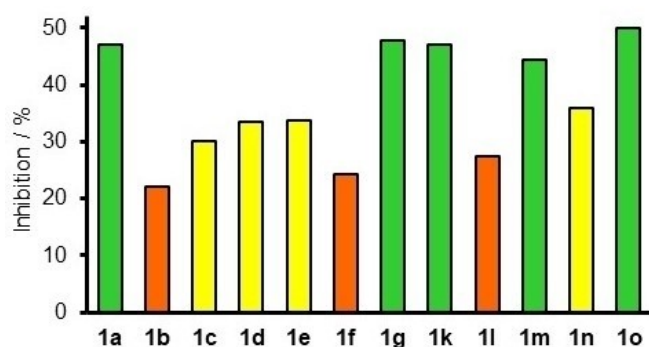


Figure 3. Inhibition screening for compounds **1** (1 μM) with insulin receptor substrate IRS5 as PTP1B substrate.

an *IC*₅₀ in the sub-micromolar range (Table 1 and Figure S1 in the Supporting Information).

T-cell protein tyrosine phosphatase (TCPTP) is the human tyrosine phosphatase with the highest degree of homology (ca. 75%) with PTP1B, thus making this enzyme a good control to assess the selectivity of inhibition. As such, the *IC*₅₀ was determined for human TCPTP (63.2 kDa; 1.6 nM) with our best inhibitors (*IC*_{50/PTP1B} < 2 μM) using conditions strictly identical to those used for PTP1B. The selectivity indices (*IC*_{50/TCPTP} / *IC*_{50/PTP1B}) obtained ranged from 0.5- to 44-fold (Table 1). Most of the inhibitors assayed were selective for PTP1B, especially **1 d** and **1 g**, which showed selectivity indexes (SI) higher than 41-fold. Compound **1 h** was fourfold selective, whereas **1 i** showed no selectivity. Moreover, **1 i** and **1 l** were slightly selective (1.39- and 2.1-fold, respectively) for TCPTP.

It has been suggested that a Phe280 residue in the PTP1B allosteric pocket, which is missing in TCPTP, bearing a Cys278 residue instead, could be the origin of the selective inhibition of PTP1B versus TCPTP.^[27] Recently, the selectivity of the benzbro-marone derivative allosteric inhibitor BB2 reported by Wiesmann (an analogue lacking of thiazole ring in inhibitor depicted in Figure 1, bottom left) has been investigated by computational MD and end-point free energy methods.^[28] García-Marín found that the allosteric site of TCPTP presented higher mobility (and higher fluctuations of the ligand BB2 inside the pocket) and overall flexibility than that of PTP1B. This study illustrates the crucial role that Phe280 plays in the allosteric recognition of PTP1B, and highlights the importance of hydrophobic interactions, especially sandwich π stacking, for the design of effective allosteric inhibitors of PTP1B, in terms of not only free energy but also stability of the final ligand-protein complex.

This Phe280 residue can establish π-stacking interactions with inhibitors that do not occur in TCPTP. Then, compounds having two aromatic rings separated by a chain have been reported to adopt a U-shape conformation able to doubly stack up and down Phe280 by π-π stacking interaction through a sandwich-type form (see Figure 1 bottom left). In this regard, compound **1 h** was designed to establish an additional π-stacking interaction with Phe280 as it was observed in

Table 1. [*IC*₅₀] and selectivity data for compounds **1**.

Compd.	R ¹	R ²	R ³	R ⁴	R ⁷	R ⁸	<i>IC</i> ₅₀ ± SD [μM]		SI ^[a]
							PTP1B	TCPTP	
1 a	H	H	H	Me	H	H	1.00 ± 0.01	3.95 ± 1.81	n.
1 b	H	H	H	Me	Me	Me	> 10	n.d.	n.d.
1 c	H	H	H	Me	Me	H	> 10	n.d.	n.d.
1 d	H	H	H	Me	Cl	Cl	0.57 ± 0.22	> 25	> 43.86
1 e	H	H	H	Me	Me	H	> 10	n.d.	n.d.
1 f	H	H	H	Me	OMe	H	> 10	n.d.	n.d.
1 g	H	H	H	Me	H	Cl	0.60 ± 0.11	> 25	> 41.67
1 h	H	H	H	Bn	H	H	0.24 ± 0.01	0.96 ± 0.21	4.00
1 i	H	H	H	Ph	H	H	0.62 ± 0.08	0.45 ± 0.40	0.72
1 j	H	H	H	H	H	H	0.88 ± 0.43	1.79 ± 1.01	2.03
1 k	Br	H	H	Me	Me	Me	n.s.	n.s.	n.s.
1 l	H	H	Br	Me	Me	Me	4.20 ± 0.98	1.99 ± 1.48	0.47
1 m	Br	Br	H	Me	Me	Me	n.s.	n.s.	n.s.
1 n	Br	H	H	Me	H	Cl	1.82 ± 0.94	7.95 ± 3.02	4.37
1 o	H	H	Br	Me	H	Cl	4.69 ± 0.43	n.d.	n.d.

[a] Selectivity index, SI = *IC*_{50/TCPTP} / *IC*_{50/PTP1B}; n.d.: not determined; n.s.: not soluble; Experiments were carried out in duplicate (N = 3).

molecular docking experiments (see Computational Approach section). Surprisingly, inhibitors **1d** and **1g**, which lack the benzyl group at C4 and bear chlorine atoms at C7/C8, showed the highest selectivity with selectivity indexes (SI) above 40, which is tenfold the SI for **1h**. Then, the origin of the selectivity of inhibitors **1d** and **1g** cannot be explained by π -stacking interactions only.

Structure-activity relationships

To better explain the IC_{50} data (Table 1), we considered three sets of inhibitors: potent ($IC_{50} < 2 \mu\text{M}$), good ($2 < IC_{50} < 10 \mu\text{M}$) and poor ($IC_{50} > 10 \mu\text{M}$). Although the IC_{50} dataset is small, some qualitative structure-activity relationships can be extracted. Thus, only hydrogen or chlorine atoms at R^7 are allowed in domain 1 (Figure 2), with a chlorine atom favouring inhibition (**1d** vs **1g**). In contrast, bulkier substituents such as methyl, trifluoromethyl and methoxy are detrimental to the activity (**1a** vs **1c**, **1e**, and **1f**). A chlorine atom at R^8 improves activity slightly (**1a** vs **1g**) but has no effect if R^7 is substituted by chlorine (**1d** vs **1g**). In domain 2, the introduction of a bromine atom pursued to mimic the bromine atoms as in benzbromarone-derived allosteric inhibitors (Figure 1, bottom left). However, a bromine atom diminishes the activity and the detrimental effect is stronger at R^3 (**1g** vs **1o**) than at R^1 (**1g** vs **1n**). In domain 3, alkyl and aryl substituents at R^4 are allowed and their activity follows the hierarchical order Bn (**1h**) > Ph (**1i**) > H (**1j**) \geq Me (**1a**).

For selectivity against TCPTP, and despite the small dataset available, we found that a chlorine atom at R^8 is essential (**1a** vs **1g**), whereas another chlorine atom at R^7 has poor or little effect (**1g** vs **1d**). A hydrogen atom or an alkyl group (Me, Bn) are allowed at R^4 but have little effect on selectivity (**1a** vs **1h** vs **1j**) and should not be conjugated to the ring like a phenyl group (**1i**). A bromine atom at R^1 is detrimental to selectivity (**1g** vs **1n**) by a factor of tenfold. Interestingly, two compounds (**1i** and **1l**) showed a slight preference for TCPTP, and a small inversion in selectivity is observed when a phenyl group occupies R_4 (**1i**). This reversal in selectivity also takes place for **1l**, although in this case it is not clear if the reason is the presence of a bromine atom at R^3 , methyl groups at R^7 and R^8 , or both.

Enzyme inhibition kinetics and aggregate formation

In order to disclose the inhibition mechanism that operates with these inhibitors, we performed enzyme inhibition kinetics assays with compounds **1a**, **1g** and **1h**, as representative examples of potent inhibitors with no substitution (**1a**) and a chlorine atom (**1g**) at Domain 1, and a benzyl group able to π -stacking at Domain 3, respectively. Lineweaver-Burk plot for **1a** showed an apparent mixed inhibition mechanism, although for **1g** and **1h** plots did not fit into classic inhibition mechanisms (Figures S2–S4). Experimental data could not fit to model kinetic equations, neither those considering the activation/inhibition

performed by substrate, then obtaining low correlations plots for each compound in every model.^[29,30] Unfortunately, results obtained were inconclusive. Then, we considered the possibility of aggregate formation by compounds **1a**, **1g** and **1h** for shedding light upon the problems encountered during the experiments of enzyme inhibition kinetics. Thus, to predict if these compounds are prone to aggregate, we used Aggregate Advisor tool. This tool helps to distinguish between true and artefact screening hits based on Tanimoto structural similarity index (compared to known aggregators) and on lipophilicity criteria (based on calculated $\log P$).^[31] Compound **1a** ($c\log P$ 2.9) has 73% similarity to 1-methyl- β -carboline, a known aggregator. Although this tool gives no similarities for **1g** or **1h** to known aggregators, their $c\log P$ values are high (3.5 and 4.8, respectively) and we could not rule out aggregate formation by these compounds due to their flatness and high lipophilicity.

We studied the possibility of aggregate formation by compounds **1a**, **1g** and **1h** in buffered solutions of Tris-HCl containing ~1% of DMSO by performing measurements of steady-state and time-resolved fluorescence, as well as dynamic light scattering (DLS; Figures S5–S8 and Table S1). The fluorescence emission spectra (Figure 4, left) exhibited a monomer band centred at ~306 nm and a second structureless band shifted to the red at 399, 403 and 415 nm for **1a**, **1g** and **1h**, respectively, which was attributed to the presence of aggregates presumably formed by π - π stacking interaction. The largest aggregation (which does not mean the largest aggregate size) was observed for **1a**, followed by **1h** and much less for **1g** in the normalized spectra (Figure 4, right). Experiments were performed in the same aqueous medium used in our enzyme kinetics assays. As a result, these compounds formed very stable aggregates in buffered solutions of Tris-HCl containing ~1% of DMSO at micromolar concentrations by presumable π - π stacking interactions. The presence of stable aggregates for inhibitors **1a**, **1g** and **1h**, can probably be extended to all compounds **1** due to their flatness and lipophilicity, thus providing a strong reason for the unsuccessful results obtained

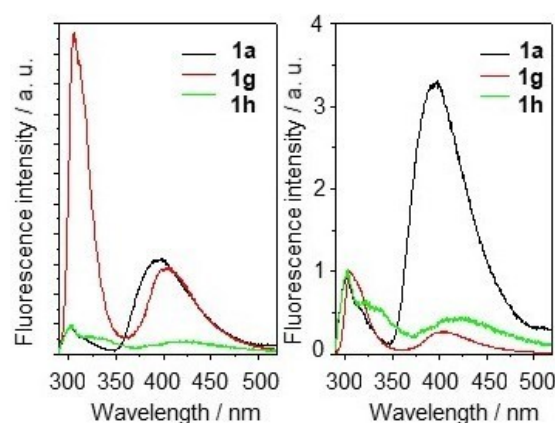


Figure 4. Emission spectra for **1a**, **1g** and **1h** derivatives in buffered solutions of Tris-HCl containing ~1% of DMSO at a 25 μM concentration (left); Emission spectra normalized to the maxima of monomer bands located around 306 nm (right). Measurements were performed at 25 $^{\circ}\text{C}$.

in experiments on enzyme inhibition kinetics. Thus, the IC_{50} and selectivity data reported herein (see former section) must be taken with caution as correspond to mixtures aggregate-aggregator where is not clear what is the inhibitory specie, the aggregator, the aggregate, an enzyme-aggregate colloid or a combination of them.

Shoichet lab and other researches as well, have largely contributed to the study of aggregates in medicinal chemistry. This is a matter of concern to the pharmaceutical community because compounds physicochemical properties in aqueous media influence drug behaviour.^[32,33] However, aggregate formation is also an opportunity to selectivity and to their use in drug-delivery.^[34–36] In particular, protein stability has implications for the binding onto aggregates and this could have an effect on selectivity.^[35] Moreover, Janssen lab hypothesized by first time that aggregates are absorbed in the intestine tract as opposed to individual molecules.^[37] In fact, approved drugs like, for instance, moxalactam, gefitinib, pranlukast, crizotinib and clofazamine, among many others, or the antioxidant (*E*)-resveratrol, are known aggregators.^[35,38,39]

Aggregates have been reported to show selective protein binding and this has been related to protein stability (the lower is the stability, the higher is the loading onto the aggregate).^[34,35] As we are reporting here (see Computational approach section), no potential PAINS (pan assay interference compounds) were found, meaning that these compounds do not show potential protein promiscuity.

On the other hand, it has been reported that aggregates can have different IC_{50} values against different proteins. This has been attributed to differences in protein concentration in the pertinent assays.^[40,41] As spectroscopic measurements showed that **1a**, **1g** and **1h** are aggregators that co-exist with aggregates, then it is not possible to attribute the activity or the selectivity of these compounds to one kind or another, even performing IC_{50} assays using strictly identical conditions, as we made. Thus, the activity and selectivity of compounds **1** needs to be addressed since it is still unclear what factors, other than π -stacking with Phe280 in PTP1B, are operating for these highly homologous enzymes, like protein conformational restraints/freedom, binding onto aggregates or both. Thus, the observed selectivity for compounds **1** needs a deeper study that is far from the aim of this work. This study is currently ongoing and results will be soon reported elsewhere.

Although the inhibition model could not be experimentally demonstrated for these compounds, we performed a computational study for the binding of the aggregator form of these inhibitors to the two major and best reported binding pockets for PTP1B inhibitors: the active site and the allosteric pocket at the $\alpha 3/ \alpha 6/ \alpha 7$ tunnel.

Computational approach

PTP1B has been intensively studied as a druggable target. Indeed, at the time of drafting this manuscript, a total of 144 crystal structures had been deposited in the Protein Data Bank (PDB), with 86 of these involving complexation to small

molecules.^[42] Two main binding modes, namely, active-site inhibition and allosteric inhibition, are found for these structures.

The active site has been reported to be an extremely conserved domain among PTPs, and inhibition with small molecules has been shown to be nonselective.^[22,43] Enhanced ligand selectivity can be achieved by allosteric binding. To assess the selectivity of the most active compounds **1** between two possible binding sites, in other words the catalytic and allosteric site, docking experiments were performed using the FlexX 4.0 module implemented in the LeadIT suite (Table S2).^[44] To model the interaction at the catalytic binding site, the crystal structure with PDB ID: 2NTA was chosen. FlexX parameters were set as default and protonation states were investigated at $pH 7.4 \pm 2$ (Table S2). All compounds showed better docking scores at the allosteric site rather than at the catalytic site. Moreover, as implausible binding modes in the active site of PTP1B were found, extensive molecular modelling studies were performed at the allosteric site. In order to evaluate the possibility that the compounds synthesized herein bind PTP1B at the allosteric site, docking calculations were carried out using the Schrödinger suite (<http://www.Schrodinger.com>). PTP1B has been crystalized with an allosteric inhibitor BB3 and this structure has been deposited in the PDB with code 1T48 (Figure 5a).^[44] This structure was used as the target protein for docking purposes. However, since it has not been completely solved (there are some residues missing in the $\alpha 7$ helix), homology modelling techniques were necessary to obtain a complete target structure. The modelled structure was obtained with SWISS-MODEL web server and 1T48 as template.^[46] Compounds **1** were directly docked inside this generated PTP1B model, with the results showing that the tricyclic system present in our ligands occupies the site of the dibromohydroxybenzoyl moiety from BB3, filling the hydrophobic pocket formed by helices $\alpha 3$, $\alpha 6$, and $\alpha 7$. All compounds establish π - π interactions with Phe196 ($\alpha 3$ helix) and Phe280 ($\alpha 6$ helix), as well as a parallel displaced interaction with Trp291 ($\alpha 7$ helix) (Figure 5b). Moreover, van der Waals interactions are established with the side chains of Leu192 and Ile281. Atom N5 from the tricyclic core hydrogen bonds to the side chain of Asn193 in all cases. Interestingly, halogen-containing compounds such as **1d**, **1g**, **1m**, **1n** and **1o** reproduce the halogen positions of the reference compound (BB3), although in **1m**, the molecule flips to place bromine atoms at the pyrrole ring instead of chlorine atoms at the benzene ring (see Figure S10). To test the stability of the proposed binding modes and rationalize the biological results described above, 20 ns molecular dynamics (MD) simulations were carried out for all complexes. Analysis of the MD trajectories highlights the stability of the docked complexes, which is in complete agreement with the experimental results, further supporting the putative allosteric site binding of this series of compounds.

The ligand stability within the binding pocket can be assessed from the low root mean square deviation (RMSD) values for the ligand atoms (Figure 6 and Table 2), which range from 0.81 to 4.49 Å. These values are, in general, in agreement with a well-stabilized, low-energy predicted binding mode. The

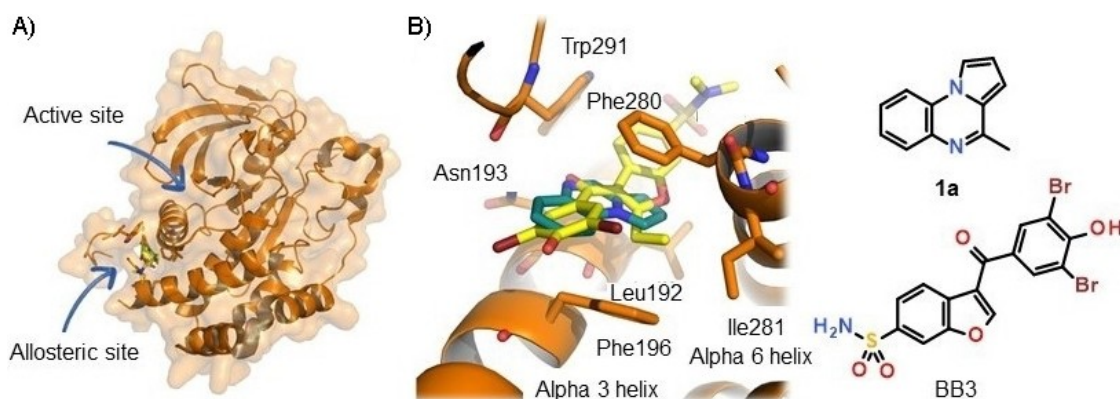


Figure 5. a) PyMOL representation of crystal structure 1T48. The protein is coloured orange, and BB3 is shown as yellow sticks. b) Superimposition of docked **1a** (pale blue) inside the PTP1B model with BB3 (yellow). The main interacting residues are represented as sticks.

Table 2. Predicted total binding energies (docking and MD simulations) and mean RMSD values for selected protein substructures and ligands along the MD simulations.

Predicted binding energy Compd.	Predicted binding energy		Mean RMSD values along 20 ns MD				WPD loop [Å]	Ligand [Å]
	Docking score [kcal/mol]	MM-ISMSA [kcal/mol]	Alpha 3 helix [Å]	Alpha 6 helix [Å]	Alpha 7 helix [Å]			
1a	-6.40	-27.19	0.397	0.289	1.121	0.635	2.393	
1b	-6.52	-31.01	0.468	0.694	1.430	0.597	2.234	
1c	-6.51	-29.70	0.423	0.519	0.967	0.733	2.039	
1d	-6.55	-32.60	0.411	0.761	0.923	0.683	0.853	
1e	-6.55	-29.46	0.444	0.575	0.545	0.624	1.161	
1f	-5.88	-23.86	0.530	0.624	3.755	0.597	2.157	
1g	-6.55	-29.41	0.453	0.828	1.217	0.562	1.081	
1h	-9.02	-33.31	0.421	0.578	0.553	0.589	2.292	
1i	-7.43	-34.51	0.402	0.483	0.733	0.624	1.201	
1j	-6.16	-24.60	0.483	0.586	0.927	0.473	1.304	
1k	-6.94	-30.62	0.468	0.720	0.509	0.545	3.348	
1l	-7.26	-33.88	0.367	0.562	1.503	0.575	1.542	
1m	-6.58	-36.15	0.507	0.547	1.023	0.537	4.496	
1n	-6.95	-29.55	0.413	0.573	0.490	0.528	2.668	
1o	-6.98	-34.10	0.695	0.995	1.498	0.541	0.815	
1T48 model		-	0.442	0.794	0.652	0.726	-	
2HNP model		-	0.3872	0.862	0.613	1.397	-	

ligands remain within the allosteric binding pocket throughout the entire simulation time and are mainly maintained by stable π -stacking interactions with Phe196 ($\alpha 3$ helix) and Phe280 ($\alpha 6$ helix) and transient van der Waals and hydrophobic interactions with Trp291, Leu192 and Ile281. However, a clear correlation between complex stability and IC_{50} cannot be obtained due to the minor structural differences in this series. It is interesting to note that the higher RMSD values correspond to compounds **1k** and **1m**, for which IC_{50} values were not determined due to their lack of solubility. In addition, to further support the predicted results, the dynamic behaviour of the $\alpha 3$, $\alpha 6$ and $\alpha 7$ helices and the WPD-loop of all complexes was compared to that of the protein without the bound ligand. To that end, two apo proteins were submitted to the same MD protocol mentioned above. These proteins were structure 1T48, after removal of the crystalized ligand BB3 and modelling of the missing amino acids, and structure 2HNP, which corresponds to the crystal structure of the protein with no bound ligand and after modelling of the missing $\alpha 7$ helix. In the case of the WPD

loop, this analysis shows an increased stability for most of the complexes when compared to the apo proteins (Table 2), with mean RMSD values along the simulation time for this substructure ranging between 0.47 and 0.73 Å for all complexes. This same analysis for the apo structures leads to RMSD values of 0.72 and 1.39 Å for the 1T48 and 2HNP models, respectively. These results may account for the restricted mobility of this WPD loop upon ligand binding, in contrast to the apo structures, where this loop appears to be more flexible. This observation further supports the already reported restriction to WPD loop movement upon ligand binding to PTP1B via the same allosteric pocket.^[42] On the other hand, the mean RMSD values throughout the MD simulation for $\alpha 6$ and $\alpha 3$ in all complexes show a similar dynamic behaviour as for the apo proteins.

In contrast, the $\alpha 7$ helix increases its mobility with respect to the modelled apo structures (1T48 and 2HNP). Thus, the RMSD values range from 0.49 to 3.75 Å in the complexes, whereas this same analysis gives a value of 0.6 Å for the

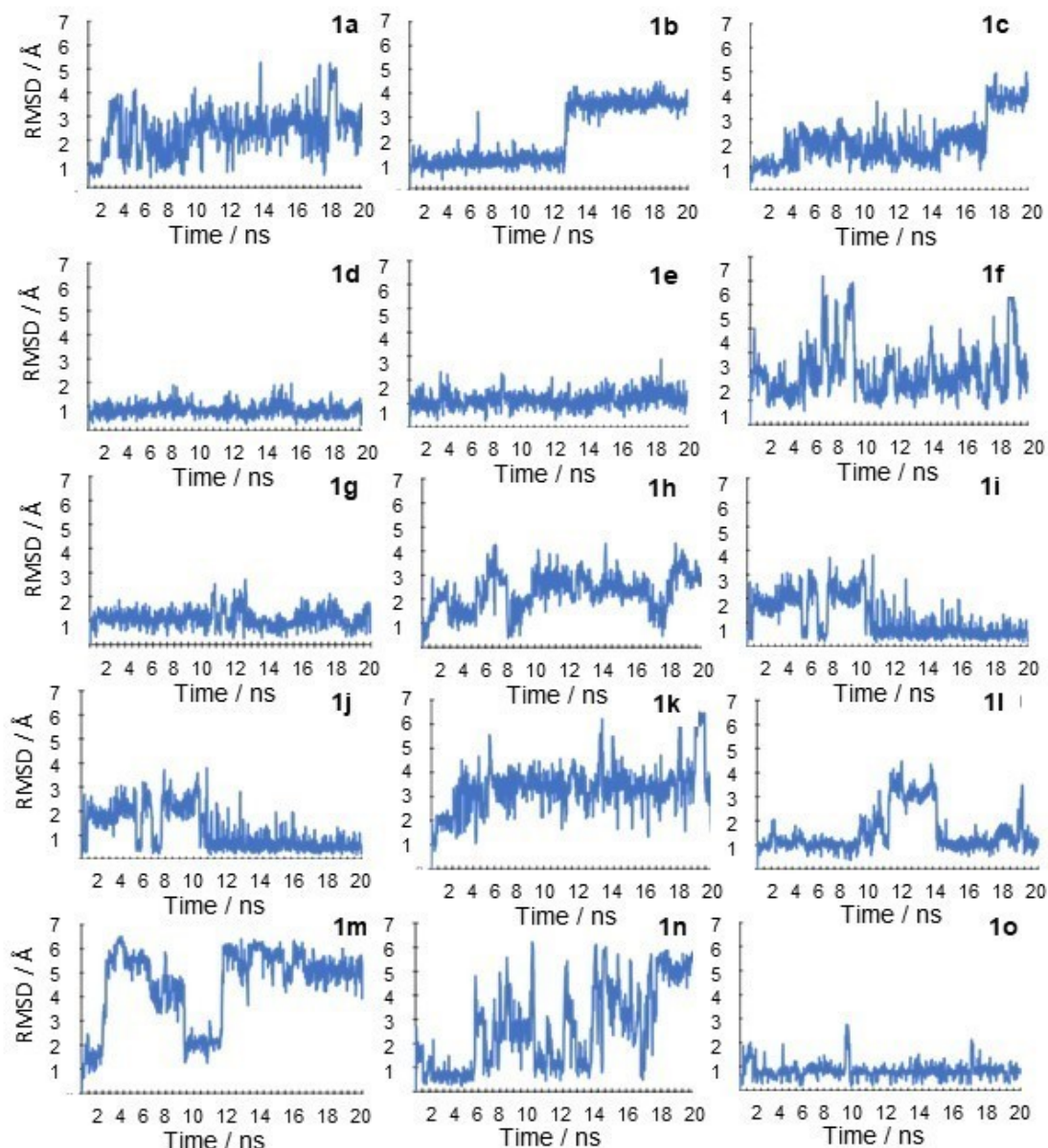


Figure 6. Evolution of the RMSD for all PTP1B-1 complexes along the 20 ns MD simulations.

modelled apo forms. These increased values in most complexes suggest a movement of the $\alpha 7$ helix which, interestingly, is in agreement with the low structured characteristics of the C-terminal end in experimentally solved allosteric complexes (e.g., PDB IDs: 1T49 and 1T4 J).^[22]

As expected for an allosteric binding mode, the WPD loop is further stabilized upon ligand binding and $\alpha 7$ exhibits high mobility, as observed experimentally for the allosteric inhibitors in crystal structures such as 1T48, 1T49 and 1T4 J.^[22,47] Taken together, these results further support a putative allosteric binding mode for this series of compounds.

In summary, our simulations provide information regarding the putative binding mode for this type of ligand but do not allow us to scrutinize this series of compounds in any greater

depth as the minor structural differences between them are not sufficient to significantly affect the binding mode to the target protein. However, our calculations strongly support the conformational rearrangement of secondary structural elements observed experimentally for this type of inhibitor.^[22,45]

To better rationalize the in vivo results (see section below: Analysis of the effects in cells), the physicochemical properties and ADME parameters were calculated using the versatile web server SWISS-ADME.^[48] All compounds showed similar physicochemical properties and ADME parameters (Table 3), with no marked differences between them. Interestingly, no potential PAINS (pan assay interference compounds) were found and the iLOGP values obtained (close to 3) correspond to improved glucose uptake (1h, 1l and 1o).^[49,50] Ligand efficiency indices

Table 3. Calculated properties: molecular weight (MW), topological polar surface area (TPSA), $i\log P$ (inhouse $\log P$), pIC_{50} values (calculated from experimental IC_{50} values), binding efficiency index (BEI) and surface binding efficiency index (SEI).

Compd.	MW [g/mol]	TPSA [\AA^2]	$i\log P$	pIC_{50}	BEI	SEI
1a	182.22	0.17	2.39	6	32.93	34.68
1b	210.27	0.17	2.84	5	23.78	28.90
1c	196.25	0.17	2.63	5	25.48	28.90
1d	251.11	0.17	2.82	6.24	24.85	36.07
1e	250.22	0.17	2.67	5	19.98	28.90
1f	212.25	0.26	2.64	5	23.56	18.85
1g	216.67	0.17	2.67	6.22	28.71	35.95
1h	258.32	0.17	2.97	6.61	25.59	38.21
1i	244.29	0.17	3.02	6.2	25.38	35.84
1j	168.19	0.17	2.11	6.05	35.97	34.97
1k	289.17	0.17	3.09	–	–	–
1l	289.17	0.17	3.14	5.37	18.57	31.04
1m	289.17	0.17	3.39	–	–	–
1n	295.56	0.17	2.91	5.73	19.39	33.12
1o	295.56	0.17	2.96	5.32	18.00	30.75

were also calculated using the binding efficiency index (BEI) and surface binding efficiency index (SEI) based on the molecular weight (MW) and topological polar surface area (TPSA).^[51] As reported in the literature, the BEI and SEI values should be around 27 and 18, respectively, for a compound to be considered a good druggable lead. In general, the values for our compounds are close to those reported previously, although the SEI values are farther from the canonical ones. However, according to the literature, the suitability of a series of compounds to be considered as druggable leads should be assessed from either BEI or SEI. Therefore, in this case, we can further confirm that the reported series constitute a good starting point for the development of allosteric PTP1B inhibitors. Taken together, our results point to future strategies for lead optimization of this series by appropriate growth of the lead structure via the pyrrole end in order to sandwich Phe280, as demonstrated for BB3.

Screening of cell viability

The determination of IC_{50} against PTP1B and TCPTP allowed us to identify two potent and very selective inhibitors (1d and 1g) and three good and slightly selective inhibitors (1a, 1h and 1n). After these promising results, the cell viability was screened. Compounds 1 were tested using the MTT assay on HepG2 and C2C12 (for the most potent inhibitors tested on cell glucose metabolism) cell lines at 50 μM . Both cell lines showed high viability (>90%) towards these compounds (Figure 7).

Analysis of the effects in cells

We tested the effect of some inhibitors in C2C12 cells to validate the potential therapeutic use of these inhibitors. These cells are derived from mouse muscle myoblasts and constitute a good target for assessing the effects of insulin. As shown in Figure 8 (panel A), all compounds tested, except 1a, induced an

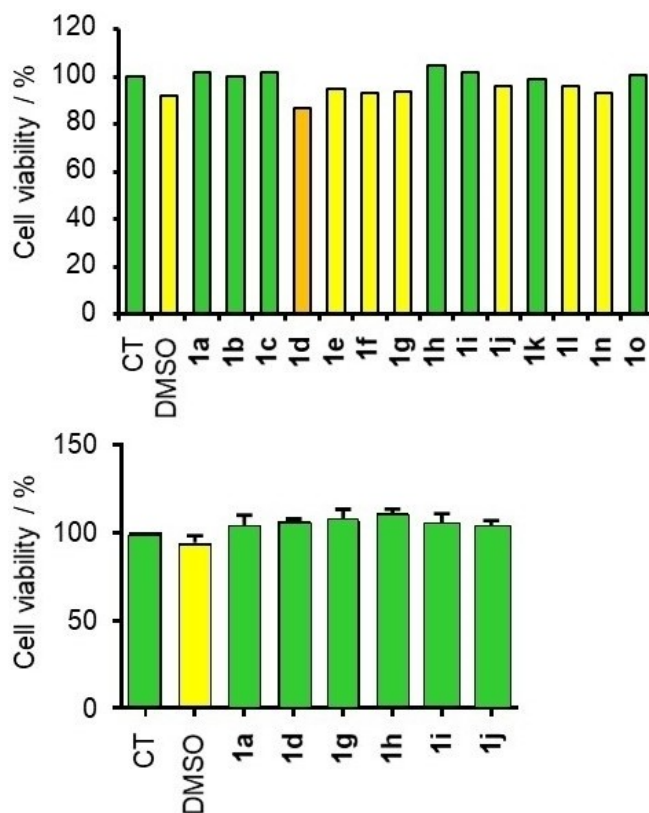


Figure 7. Viability of HepG2 (top) and C2C12 (bottom) cell lines, as determined by using the MTT assay after incubation for 24 h with compounds 1 at 50 μM . Values are expressed as percent of CT and as the mean \pm SEM of three independent experiments in duplicate.

increased glucose uptake by cells, with this effect being more relevant for compounds 1g, 1h, 1l and 1o. Compounds 1h, 1l and 1o reached the level produced by insulin. Compound 1g also increased glucose uptake, but to a slightly lesser degree than former compounds. Compound 1d increased the level of glucose uptake, although below the level reached by 1g.

An inspection of data provided by cell glucose uptake assay (expressed as percent of control) and $i\log P$ data of tested compounds (see former section) allowed us to find a qualitative relationship between both. Then, the hierarchical order found for glucose uptake test was: 1h (205%) \approx 1l (207%) \approx 1o (209%) > 1g (184%) > 1d (118%) > 1a (73%), and for $i\log P$: 1h (2.97) \approx 1l (3.14) \approx 1o (2.96) > 1d (2.82) > 1g (2.67) > 1a (2.39). Then, the higher is the lipophilicity, the biggest is the uptake of glucose by C2C12 cells, with the most potent inhibitor 1h (0.24 μM) among those producing the highest effect.

Additionally, 1h induced and increased phosphorylation of the insulin receptor substrate 1 (IRS1; panel B) and AKT (panel C), as was also the case for insulin. Combined treatment with 1h and insulin induced an additive effect on IRS1 (panel B) and AKT (panel C) phosphorylation. This same compound did not modify STAT3 phosphorylation (panel D). At peripheral nervous system, the JAK/STAT pathway induces glucose uptake in muscle via STAT3 phosphorylation by JAK, STAT3 translocation and further gene transcription. Then, our results suggest that

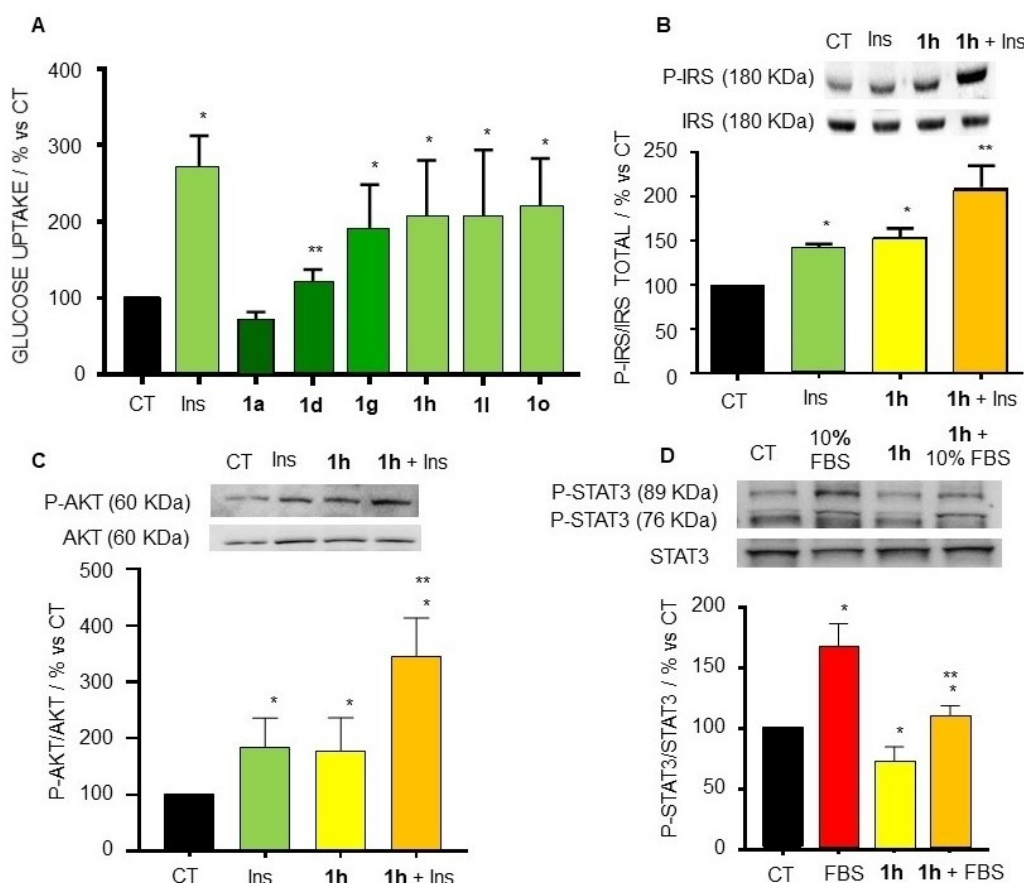


Figure 8. Biological effects on C2C12 cells. A) Effect of inhibitors **1** on glucose uptake. Effect of **1h** on the phosphorylation of B) insulin receptor substrate 1 (IRS1); C) AKT and D) STAT3. Keys: CT (control conditions, 1% DMSO); Ins (with 10 nM insulin final concentration, 30 min); **1h** (with 2 μ M inhibitor final concentration, 90 min); FBS (with 10% foetal bovine serum, 30 min). For B, C and D, representative western blots for both the phosphorylated and total proteins are shown in the upper part of the panels, and the ratios of the densitometric analysis for both signals are given in the lower part. Values are expressed as percent of CT and as the mean \pm SEM of three independent experiments (in duplicate for glucose uptake). * $p < 0.05$ vs. CT, ** $p < 0.05$ vs. the other groups (CT and Ins for glucose uptake).

the increase of glucose uptake provided by inhibition of PTP1B by **1h** in C2C12 cells is not due to changes in the phosphorylated status of STAT3, but rather due to the inhibition of pAKT dephosphorylation, then promoting the insulin-induced translocation of glucose transporter 4 (GLUT4) to the plasma membrane.

Conclusion

We have reported the discovery of pyrrolo[1,2-*a*]quinoxalines as scaffolds that provide potent and selective PTP1B inhibitors with insulin mimetic properties. This scaffold putatively binds to the allosteric hydrophobic pocket formed by $\alpha 3/\alpha 6/\alpha 7$ helices, as supported by molecular docking and molecular dynamics simulations. A set of 15 compounds bearing substituents at three domains, namely the benzene, pyrrole and pyrazine rings, have been prepared. The inhibitory activity of these compounds ranges from 0.24 to 4.69 μ M, their selectivity indices against TCPTP are in the range >44-fold to 0.47-fold and they are nontoxic to HepG2 or C2C12 cells. The best inhibitors bear

hydrogen or chlorine atoms at C-7 and C-8, hydrogen atoms in the pyrrole ring and benzyl or phenyl groups at C-4 to establish π interactions with Phe196 and Phe280. Molecular docking and molecular dynamics studies using the PTP1B homology model support binding to the $\alpha 3/\alpha 6/\alpha 7$ pocket, thereby stabilizing the WPD loop in an open, non-catalytic conformation. The inhibition mode could not be revealed since enzyme inhibition kinetics assays were unsuccessful due to aggregate formation, as it has been proven by fluorescence and DLS methods applied to **1a**, **1g** and **1h**. The inhibitors tested showed enhanced glucose uptake comparable to insulin when their $i \log P$ value is close to 3, as for **1h**, **1l** and **1o**, and showed no effect when $i \log P$ is, at least, below 2.4. Compound **1h**, which is one of best inhibitors, also inhibits pIRS and pAKT dephosphorylation in C2C12 cells, and enhances the insulin-dependent phosphorylation of these proteins, while STAT3 phosphorylation was not modified by **1h**. ADME properties and druggability indices were also calculated, thereby further supporting the suitability of the compounds as leads for inhibition of PTP1B by a putative allosteric mechanism.

Experimental Section

Chemistry

Solvents (HPLC quality, Scharlau) were dried in a Solvent Purification System (MBraun) by passing through a pre-activated alumina column or were purchased as anhydrous quality. Reagents were purchased from Merck/Sigma-Aldrich or Acros and were used as received. Reactions were monitored by thin-layer chromatography (TLC) on silica-coated aluminium sheets (Alugram silica gel 60 F254). Spots were visualized by UV light (254 nm). Column chromatography was carried out with Merck silica gel (0.030–0.075 mm) and solvents were used as received (Scharlau). Infrared spectra (IR, NaCl windows or KBr pellets) were recorded on a Perkin-Elmer FTIR 1725X instrument. Frequencies (ν) of the more intense bands are given in cm^{-1} . Nuclear magnetic resonance spectra (^1H and ^{13}C NMR) were recorded using a Varian Gemini 200 (200 and 50 MHz, respectively), Varian UNITY-300 (300 and 75 MHz, respectively), Varian Mercury-VX-300 MHz and Varian-UNITYPLUS-500 (500 and 125 MHz, respectively) instruments. Chemical shifts (δ) are given in ppm and are referenced to the residual signal of the non-deuterated solvent. Coupling constants (J) are given in Hz. All compounds were analysed by tandem HPLC-MS. HPLC was performed on a reverse-phase C_{18} column (Luna, Phenomenex, 3 μm , 3 \times 100 mm) using a gradient of MeOH/water/4% formic acid at a flow rate of 1.0 mL min^{-1} . Products were detected at $\lambda = 254$ nm. Compounds were $\geq 95\%$ pure. Mass spectra were recorded on a Hewlett-Packard 5988 A mass spectrometer. High-resolution mass spectra were recorded on an Agilent 6210 LC/MS TOF mass spectrometer.

The synthesis of compounds **3**, **4**, **5** and **6** is reported in SI. The synthesis of compounds **1** is reported below.

Synthesis of pyrrolo[1,2-*a*]quinoxalines (**1**)

General procedure A: A mixture of acetanilide **5** or *N*-acetylacetanilide **6** (3–13 mmol) and POCl_3 (5 mL/mmol) was heated at reflux temperature. Next, the reaction mixture was cooled to room temperature and evaporated to dryness. Iced water (20 mL/mmol) was added over the resulting residue and the pH was adjusted to 7–8 with 5% NaHCO_3 . The mixture was extracted with CH_2Cl_2 (3 \times 30 mL/mmol) and the organic extracts were pooled and dried (MgSO_4). The desiccant was filtered off and the solvent was removed under reduced pressure to give a residue that was chromatographed on silica gel using CH_2Cl_2 /acetone 9:1 as eluent.

General procedure B: Compound **4** (0.312 mmol) was dissolved in trimethyl orthoformate (0.8 mL/mmol). Some drops of AcOH were added and the solution was stirred at reflux for 1.5 h. Next, water (10 mL/mmol) was added and the mixture was extracted with CH_2Cl_2 (3 \times 16 mL/mmol). Organic extracts were washed with brine (16 mL/mmol), dried over Na_2SO_4 , filtered and evaporated under reduced pressure to afford a brown solid. The solid was dissolved in MeOH, water was added dropwise and the precipitate was filtered and dried.

4-Methylpyrrolo[1,2-*a*]quinoxaline (1a). General procedure A. Compound **5a** (2.18 g, 10.9 mmol) was heated for 1.25 h. Yield: 1.77 g (89%); brown solid; mp: 138–140 °C; IR (ν_{max} KBr): 3439, 3099, 1611, 1529, 1481, 1416, 1380, 1361, 1323, 1258, 1212, 1042, 947, 859, 760, 732, 690, 650, 609, 534, 470 cm^{-1} ; ^1H NMR (200 MHz, CDCl_3): $\delta = 7.89$ (m, 2H), 7.82 (dd, 1H, $J = 7.4$ Hz, $J = 2.3$ Hz), 7.43 (m, 2H), 6.88 (dd, 1H, $J = 4.2$ Hz, $J = 1.3$ Hz), 6.83 (t, 1H, $J = 3.2$ Hz), 2.72 (s, 3H) ppm.

4,7,8-Trimethylpyrrolo[1,2-*a*]quinoxaline (1b). General procedure A. Compound **5b** (2.89 g, 12.8 mmol) was heated for 1 h. Yield: 2.43 g

(91%); yellow solid; mp: 137–139 °C; IR (ν_{max} KBr): 3435, 3116, 2919, 1625, 1523, 1490, 1412, 1351, 1313, 1244, 1086, 1024, 888, 853, 748, 717, 603 cm^{-1} ; ^1H NMR (300 MHz, CDCl_3): $\delta = 7.77$ (dd, 1H, $J = 2.6$ Hz, $J = 1.2$ Hz, H-1), 7.62 (s, 1H, H-6/H-9), 7.51 (s, 1H, H-9/H-6), 6.78 (m, 2H, H-2, H-3), 2.67 (s, 3H, CH_3), 2.38 (s, 3H, CH_3), 2.34 (s, 3H, CH_3) ppm; ^{13}C NMR (75 MHz, CDCl_3): $\delta = 152.3$, 136.1, 134.0, 133.7, 129.3, 126.1, 125.1, 113.9, 113.5, 112.9, 105.7, 21.9, 20.1, 19.6 ppm; HRMS [ESI-TOF] m/z calcd for $\text{C}_{14}\text{H}_{15}\text{N}_2$ [$M+H$] + 211.1230, found [$M+H$] + 211.1200.

4,7-Dimethylpyrrolo[1,2-*a*]quinoxaline (1c). General procedure A. Compound **5c** (0.65 g, 3.05 mmol) was heated for 50 min. Yield: 0.46 g (77%); yellow solid; mp: 271–273 °C; IR (ν_{max} KBr): 3423, 3095, 2624, 1885, 1624, 1598, 1550, 1507, 1405, 1377, 1285, 1260, 1111, 1046, 823, 753, 679, 601, 530 cm^{-1} ; ^1H NMR (300 MHz, CDCl_3): $\delta = 8.38$ (s, 1H, H-6), 8.21 (dd, 1H, $J = 2.6$ Hz, $J = 1.6$ Hz, H-1), 7.83 (d, 1H, $J = 8.2$ Hz, H-9), 7.47 (m, 2H, H-3, H-8), 7.13 (dd, 1H, $J = 4.6$ Hz, $J = 2.6$ Hz, H-2), 3.16 (s, 3H, CH_3), 2.52 (s, 3H, CH_3) ppm; ^{13}C NMR (75 MHz, CDCl_3): $\delta = 152.5$, 136.7, 129.7, 125.6, 124.9, 124.4, 117.9, 115.6, 113.8, 113.8, 111.7, 21.1, 19.5 ppm; HRMS (ESI+) m/z calcd for $\text{C}_{13}\text{H}_{13}\text{N}_2$ [$M+H$] + 197.1079, found [$M+H$] + 197.1074.

7,8-Dichloro-4-methylpyrrolo[1,2-*a*]quinoxaline (1d). General procedure A. Compound **5d** (2.69 g, 10 mmol) was heated for 45 min. Yield: 2.49 g (99%); brown solid; mp: 197–199 °C; IR (ν_{max} KBr): 3448, 3093, 2925, 2362, 1718, 1606, 1478, 1409, 1298, 1216, 1130, 1048, 879, 852, 745, 639, 604, 545 cm^{-1} ; ^1H NMR (500 MHz, CDCl_3): $\delta = 7.93$ (s, 1H, H-6/H-9), 7.81 (s, 1H, H-9/H-6), 7.75 (dd, 1H, $J = 2.7$ Hz, $J = 1.3$ Hz, H-1), 6.90 (dd, 1H, $J = 4.0$ Hz, $J = 1.3$ Hz, H-3), 6.84 (dd, 1H, $J = 4.0$ Hz, $J = 2.7$ Hz, H-2), 2.68 (s, 3H, CH_3) ppm; ^{13}C NMR (75 MHz, CDCl_3): $\delta = 154.9$, 134.7, 130.5, 129.8, 128.7, 126.2, 125.8, 115.2, 115.1, 114.5, 108.1, 21.7 ppm; HRMS (ESI+) m/z calcd for $\text{C}_{12}\text{H}_9\text{Cl}_2\text{N}_2$ [$M+H$] + 251.0137, found [$M+H$] + 251.0158.

7-Trifluoromethyl-4-methylpyrrolo[1,2-*a*]quinoxaline (1e). General procedure A. Compound **5e** (0.96 g, 3.59 mmol) was heated for 40 min. Yield: 0.88 g (98%); brown solid; mp: 128–130 °C; IR (ν_{max} KBr): 3104, 1628, 1530, 1504, 1459, 1420, 1334, 1299, 1208, 1164, 1142, 1108, 1089, 1033, 899, 828, 766, 737, 696, 653, 606, 526 cm^{-1} ; ^1H NMR (300 MHz, CDCl_3): $\delta = 8.17$ (s, 1H, H-6), 7.92 (d, 1H, $J = 2.6$ Hz, H-1), 7.88 (d, 1H, $J = 8.6$ Hz, H-9), 7.67 (d, 1H, $J = 8.6$ Hz, H-8), 6.94 (d, 1H, $J = 3.6$ Hz, H-3), 6.89 (t, 1H, $J = 3.2$ Hz, H-2), 2.73 (s, 3H, CH_3) ppm; ^{13}C NMR (75 MHz, CDCl_3): $\delta = 155.0$, 135.3, 129.1, 127.0 (q, $^2J_{\text{CF}} = 32.8$ Hz), 126.5 (q, $^3J_{\text{CF}} = 3.7$ Hz), 126.1, 123.9 (q, $^1J_{\text{CF}} = 271.7$ Hz), 123.1 (q, $^3J_{\text{CF}} = 3.7$ Hz), 114, 114.4, 114.1, 107.5, 21.8 ppm; HRMS (ESI+) m/z calcd for $\text{C}_{13}\text{H}_9\text{F}_3\text{N}_2$ [$M+H$] + 251.0791, found [$M+H$] + 251.0752.

4-Methyl-7-methoxypyrrrolo[1,2-*a*]quinoxaline (1f). General procedure A. Compound **5f** (1.61 g, 7 mmol) was heated for 35 min. Yield: 1.38 g (93%); brown solid; mp: 49–50 °C; IR (ν_{max} KBr): 3085, 1616, 1593, 1524, 1491, 1350, 1300, 1259, 1246, 1198, 1161, 1048, 1030, 932, 877, 847, 770, 717, 621 cm^{-1} ; ^1H NMR (300 MHz, CDCl_3): $\delta = 7.81$ (dd, 1H, $J = 2.3$ Hz, $J = 1.3$ Hz, H-1), 7.71 (d, 1H, $J = 8.9$ Hz, H-9), 7.37 (d, 1H, $J = 2.6$ Hz, H-6), 7.06 (dd, 1H, $J = 8.9$ Hz, $J = 2.6$ Hz, H-8), 6.85 (dd, 1H, $J = 3.9$ Hz, $J = 1.3$ Hz, H-3), 6.79 (dd, 1H, $J = 3.9$ Hz, $J = 2.6$ Hz, H-2), 3.88 (s, 3H, CH_3), 2.71 (s, 3H, CH_3) ppm; ^{13}C NMR (75 MHz, CDCl_3): $\delta = 157.0$, 153.9, 136.8, 125.9, 121.5, 115.9, 114.5, 113.9, 113.2, 110.5, 106.3, 55.6, 21.9 ppm; HRMS [ESI-TOF] m/z calcd for $\text{C}_{13}\text{H}_{13}\text{N}_2\text{O}$ [$M+H$] + 213.1028, found [$M+H$] + 213.1023.

8-Chloro-4-methylpyrrolo[1,2-*a*]quinoxaline (1g). General procedure A. Compound **5g** (2.52 g, 10.7 mmol) was heated for 40 min. Yield: 2.03 g (87%); yellow solid; mp: 143–144 °C; IR (ν_{max} KBr): 3099, 1610, 1530, 1476, 1458, 1418, 1381, 1351, 1312, 1253, 1210, 1130, 1118, 1085, 1036, 862, 846, 814, 793, 740, 677, 614, 570, 514, 463 cm^{-1} ; ^1H NMR (300 MHz, CDCl_3): $\delta = 7.79$ (m, 3H, H-1, H-6, H-9), 7.34 (dd, 1H, $J = 8.6$ Hz, $J = 2.3$ Hz, H-7), 6.88 (dd, 1H, $J = 3.9$ Hz, $J = 1.3$ Hz, H-3),

6.84 (q, 1H, $J=2.8$ Hz, H-2), 2.69 (s, 3H, CH₃) ppm; ¹³C NMR (75 MHz, CDCl₃): $\delta=153.8, 134.4, 132.2, 130.3, 127.8, 126.1, 125.4, 114.4, 114.0, 113.8, 107.0, 21.9$ ppm; HRMS (ESI+) m/z calcd for C₁₂H₉ClN₂ [M+H]⁺ 217.0527, found [M+H]⁺ 217.0551.

4-Benzylpyrrolo[1,2-*a*]quinoxaline (1h). General procedure A. Compound **5h** (36 mg, 0.13 mmol) was heated for 3 h. Yield: 29 mg (90%); White solid; mp, 90–93 °C; ¹H NMR (500 MHz, CDCl₃): $\delta=7.99$ (d, $J=7.8$ Hz, 1H), 7.88 (dd, $J=2.7, 1.2$ Hz, 1H), 7.82 (dd, $J=8.1, 1.4$ Hz, 1H), 7.50 (dd, $J=7.3, 1.5$ Hz, 1H), 7.46–7.41 (m, 3H), 7.31–7.25 (m, 2H), 7.23–7.17 (m, 1H), 6.86 (dd, $J=3.9, 0.9$ Hz, 1H), 6.80 (dt, $J=8.7, 4.3$ Hz, 1H), 4.38 (s, 2H) ppm; ¹³C NMR (125 MHz, CDCl₃): $\delta=155.38, 138.12, 129.85, 128.99, 128.65, 128.64, 127.49, 127.37, 126.72, 125.99, 125.27, 114.38, 113.83, 113.76, 107.30, 42.72$ ppm; HRMS (ESI+) m/z calcd for C₁₈H₁₄N₂ [M+H]⁺ 258.1238, found [M+H]⁺ 258.1242.

4-Phenylpyrrolo[1,2-*a*]quinoxaline (1i). General procedure A. Compound **5i** (78 mg, 0.33 mmol) was heated for 3 h. Yield: 63 mg (70%); White solid; mp, 85–87 °C; ¹H NMR (300 MHz, CDCl₃): $\delta=8.07$ (d, $J=7.6$ Hz, 1H), 8.04–7.97 (m, 2H), 7.87 (d, $J=7.7$ Hz, 1H), 7.63–7.38 (m, 5H), 7.01 (d, $J=3.7$ Hz, 1H), 6.96–6.81 (m, 1H) ppm; ¹³C NMR (125 MHz, CDCl₃): $\delta=154.4, 238.4, 136.2, 130.2, 129.7, 129.1, 128.5, 128.3, 128.0, 127.1, 125.4, 114.5, 114.0, 113.6, 108.6$ ppm; HRMS (ESI+) m/z calcd for C₁₇H₁₂N₂ [M+H]⁺ 244.1000, found [M+H]⁺ 244.0983.

Pyrrolo[1,2-*a*]quinoxaline (1j). General procedure B from **4a** (50 mg, 0.312 mmol); Yield: 52 mg (89%); cream-coloured solid; mp: 129–130 °C; cream-coloured solid; ¹H NMR (500 MHz, CDCl₃): $\delta=8.81$ (s, 1H), 8.00–7.91 (m, 2H), 7.87 (dd, $J=8.1$ Hz, $J=1.2$ Hz, 1H), 7.57–7.49 (m, 1H), 7.45 (td, $J=7.6$ Hz, $J=1.4$ Hz, 1H), 6.93–6.85 (m, 2H) ppm; HRMS (ESI+) m/z calcd for C₁₁H₈N₂ [M+H]⁺ 168.0687, found [M+H]⁺ 168.0718.

Bromination of pyrrolo[1,2-*a*]quinoxalines 1. General procedure: A solution of NBS (2–2.5 mmol) in DMF (5.6 mL/mmol) was added over a solution of **1** (2–2.5 mmol) in DMF (7.2 mL/mmol) cooled at –10 °C at a speed of 0.17 mL/min. Next, the reaction mixture was allowed to reach room temperature and satd NaCl (15 mL/mmol) was added. The mixture was then extracted with CH₂Cl₂ (5 × 15 mL/mmol) and the organic extracts were pooled and dried (MgSO₄). The desiccant was filtered off and the solvent was removed under reduced pressure to give a residue that was chromatographed on silica gel using hexane/AcOEt 9:1 as eluent.

1-Bromo-4,7,8-trimethylpyrrolo[1,2-*a*]quinoxaline (1k), 3-bromo-4,7,8-trimethylpyrrolo[1,2-*a*]quinoxaline (1l) and 1,2-dibromo-4,7,8-trimethylpyrrolo[1,2-*a*]quinoxaline (1m). From **1b** (0.40 g, 1.94 mmol). Compound **1k**: Yield, 0.29 g (52%); cream-coloured solid; mp: 139–140 °C; IR (ν_{max} , KBr): 3435, 2970, 2915, 1682, 1623, 1579, 1530, 1478, 1411, 1380, 1352, 1218, 1154, 1042, 912, 883, 857, 764, 735, 684, 674 cm⁻¹; ¹H NMR (500 MHz, CDCl₃): $\delta=9.00$ (s, 1H, H-9), 7.64 (s, 1H, H-6), 6.82 (d, 1H, $J=4.2$ Hz, H-3), 6.78 (d, 1H, $J=4.2$ Hz, H-2), 2.64 (s, 3H, CH₃), 2.41 (s, 3H, CH₃), 2.36 (s, 3H, CH₃) ppm; ¹³C NMR (75 MHz, CDCl₃): $\delta=152.3, 136.6, 134.4, 133.6, 129.3, 125.0, 122.7, 116.8, 113.4, 113.3, 93.8, 24.3, 20.2, 19.5$ ppm; HRMS (ESI+) m/z calcd for C₁₄H₁₄N₂Br [M+H]⁺ 289.0340, found [M+H]⁺ 289.0338; Compound **1l**: Yield, 0.21 g (39%); yellow solid; mp: 190–192 °C; IR (ν_{max} , KBr): 3434, 3108, 2966, 2918, 1708, 1621, 1576, 1512, 1485, 1408, 1376, 1342, 1218, 1137, 1098, 1007, 975, 917, 882, 853, 758, 735, 691, 673, 605 cm⁻¹; ¹H NMR (200 MHz, CDCl₃): $\delta=7.70$ (d, 1H, $J=2.5$ Hz, H-1), 7.57 (s, 1H, H-6), 7.45 (s, 1H, H-9), 6.78 (d, 1H, $J=2.5$ Hz, H-2), 2.93 (s, 3H, CH₃), 2.37 (s, 3H, CH₃), 2.33 (s, 3H, CH₃) ppm; ¹³C NMR (75 MHz, CDCl₃): $\delta=151.6, 135.1, 134.4, 129.4, 128.0, 126.5, 118.2, 115.6, 115.5, 106.7, 98.4, 21.5, 20.5, 19.4$ ppm; HRMS [ESI-TOF] m/z calcd for C₁₄H₁₄N₂Br [M+H]⁺ 289.0340, found [M+H]⁺ 289.0345; Compound **1m**: Yield, 0.10 g (8%); brown solid; mp:

177–178 °C. IR (ν_{max} , KBr): 3434, 3121, 2914, 1574, 1486, 1475, 1436, 1403, 1341, 1192, 1160, 1013, 881, 855, 802, 676, 564 cm⁻¹; ¹H NMR (300 MHz, CDCl₃): $\delta=8.93$ (s, 1H, H-9/H-6), 7.62 (s, 1H, H-3), 6.84 (s, 1H, H-6/H-9), 2.93 (s, 3H, CH₃), 2.39 (s, 3H, CH₃), 2.34 (s, 3H, CH₃) ppm; ¹³C NMR (75 MHz, CDCl₃): $\delta=151.6, 135.6, 135.1, 129.3, 126.5, 125.1, 121.8, 117.6, 115.8, 115.5$ (2 C), 24.6, 20.5, 19.4 ppm; HRMS [ESI-TOF] m/z calcd for C₁₄H₁₃BrN₂ [M+H]⁺ 368.9420, found [M+H]⁺ 368.9429.

1-Bromo-8-chloro-4-methylpyrrolo[1,2-*a*]quinoxaline (1n) and 3-bromo-8-chloro-4-methylpyrrolo[1,2-*a*]quinoxaline (1o). From **1g** (0.51 g, 2.37 mmol). Compound **1n**: Yield, 0.47 g (69%); yellow solid; mp: 193–194 °C. IR (ν_{max} , KBr): 3127, 2919, 1607, 1532, 1468, 1418, 1375, 1095, 1049, 849, 819, 763, 755, 678, 577, 460 cm⁻¹; ¹H NMR (500 MHz, CDCl₃): $\delta=9.25$ (d, 1H, $J=2.1$ Hz, H-9), 7.80 (d, 1H, $J=8.7$ Hz, H-6), 7.40 (dd, 1H, $J=8.7$ Hz, $J=2.1$ Hz, H-7), 6.88 (d, 1H, $J=4.2$ Hz, H-3), 6.85 (d, 1H, $J=4.2$ Hz, H-2), 2.66 (s, 3H, CH₃) ppm; ¹³C NMR (75 MHz, CDCl₃): $\delta=152.9, 135.5, 131.1, 130.3, 128.9, 127.9, 125.9, 119.0, 115.2, 107.6, 99.4, 21.5$ ppm; HRMS (ESI+) m/z calcd for C₁₂H₉BrClN₂ [M+H]⁺ 294.9632, found [M+H]⁺ 294.9648; Compound **1o**: Yield, 84.5 mg (12%); yellow solid; mp: 180–182 °C. IR (ν_{max} , KBr): 3436, 3099, 2359, 1604, 1482, 1409, 1344, 1112, 1087, 1010, 987, 856, 819, 761, 729, 686, 568 cm⁻¹; ¹H NMR (500 MHz, CDCl₃): $\delta=7.75$ (d, 1H, $J=8.7$ Hz, H-6), 7.72 (d, 1H, $J=3.0$ Hz, H-1), 7.71 (d, 1H, $J=2.0$ Hz, H-9), 7.34 (dd, 1H, $J=8.7$ Hz, $J=2.1$ Hz, H-7), 6.86 (d, 1H, $J=3.0$ Hz, H-2), 2.94 (s, 3H, CH₃) ppm; ¹³C NMR (75 MHz, CDCl₃): $\delta=153.7, 132.6, 130.4, 130.3, 126.4, 125.9, 122.5, 117.8, 114.1, 113.2, 95.3, 24.4$ ppm; HRMS (ESI+) m/z calcd for C₁₂H₉BrClN₂ [M+H]⁺ 294.9632, found [M+H]⁺ 294.9625.

Enzyme inhibition

PTP1B inhibition screening: To test the activity of compounds **1**, inhibition assays were performed using a commercial kit ("PTP1B Tyrosine Phosphatase Drug Discovery Kit", BML-AK822 Enzo Life Sciences). This kit performs a colorimetric test that measures the phosphatase activity of purified PTP1B, based on the malachite green assay. This assay measures the inorganic phosphate released into the aqueous solution that complexes with malachite green molybdate. The absorbance of the complex at 620 nm is proportional to the concentration of free phosphate.

The inhibitor was dissolved in reagent-grade dimethyl sulfoxide (DMSO) (Sigma-Aldrich, Saint Louis, MO) for assay. The assay kit contained recombinant PTP1B and the phosphopeptide substrate (IRS5). The enzyme has an estimated K_m of 85 μM for the substrate which is used to measure PTP1B activity. PTP1B was prepared for all assays to allow for a final amount of 2.5 ng/well and IRS5 was prepared to have a final assay concentration of 75 μM . Briefly, 35 μL of assay buffer was added to each well and incubated for 15 minutes at 37 °C. Inhibitors or DMSO (10 μL) as baseline control (final concentration 1 μM) were added to each well followed by 5 μL of PTP1B (2.5 ng per well) solution. Reactions were initiated by adding 50 μL of IRS5 (final concentration 75 μM) and the plate was incubated for 30 min at 37 °C. Reactions were then terminated by adding 25 μL of the provided phosphate detection reagent and wells were agitated gently to mix. Colour was allowed to develop for 25–30 min and absorbance was read at 620 nm using a spectrophotometer.

PTP1B/TCPTP inhibitory activity (IC50): PTP1B was purchased from Enzo Life Sciences and TCPTP from Merck-Sigma Aldrich. Inhibitor concentration at 50% inhibition was measured as hydrolysis of pNPP (400 mM) at 37 °C and pH 7.5 in a 96-well plate with 100 μL /well. Buffered solution consisted of Tris-HCl (25 mM, pH 7.5), β -mercaptoethanol (2 mM), EDTA (ethylenediaminetetraacetic acid, 1 mM), and DTT (dithiothreitol, 1 mM). Increasing concentrations (0,

0.04, 0.2, 1, 5 and 10 μM) of compounds were used to determine the IC_{50} . In each experiment, the hydrolysis of pNPP was measured as an increment in absorbance at 405 nm by adding substrate solution (50 μL) to a solution consisting of inhibitor (45 μL) and enzyme (5 μL ; 60 ng/mL). The nonenzymatic hydrolysis of pNPP was corrected by measuring the increase in absorbance at 405 nm obtained in the absence of enzyme. Each data point was measured by triplicate and experiment was performed by duplicate. Parameters were calculated using SigmaPlot® (SPCC Inc., Chicago, IL).

Biological methods

MTT viability test: a) *HepG2 cell line.* Cells were seeded in 24-well plate and were treated for 24 h with the compounds. Then DMEM was supplemented with MTT (0.5 mg/mL final concentration) and the myotubes were incubated at 37 °C. After 4 h, DMSO was added to dissolve the formazan crystals. Absorbance was measured at 570 nm using a spectrophotometer.^[52,53] b) *C2C12 cell line.* Cells were seeded in 24-well, differentiated to myotubes and subsequently treated with compounds (50 μM) for 24 h. Cytotoxicity of PTP inhibitors was determined by the MTT assay. For the MTT assay, cells were incubated with 3-(4,5-dimethylthiazol-2-yl)-2,5-diphenyl tetrazolium bromide (MTT) (50 μL of 5 mg/mL in PBS, Sigma Aldrich) for 4 h at 37 °C in CO_2 incubator. The medium was removed and the purple formazan crystals formed were then dissolved by adding 500 μL of dimethyl sulfoxide (DMSO) and mixed effectively by pipetting up and down. Spectrophotometric absorbance of the purple blue formazan dye was measured using Multimode Plate Reader (Perkin Elmer) at 570 nm. Optical density of each sample was compared with control optical density.

C2C12 cell differentiation and treatment. Mouse skeletal muscle cell lines, C2C12 myoblasts (from ATCC CRL-1772TM) were routinely maintained in DMEM, supplemented with 10% heat-inactivated foetal bovine serum (FBS), 1000 UI/mL penicillin, 1000 UI/mL streptomycin and 2 mM L-Glutamine at 37 °C in humidified air containing 5% CO_2 . Differentiation was induced by switching the growth medium to DMEM supplemented with 2% horse serum (HS; differentiation medium). The differentiation medium was changed every 48 h.^[54]

Glucose uptake. To determine glucose uptake, C2C12 cells were seeded in 24-well plate. Differentiated C2C12 cells were cultured in fresh DMEM for 2 h, and then treated with DMSO (1% final concentration, 90 min), insulin (10 nM final concentration, 30 min), or compounds 1 (2 μM final concentration, 90 min) at 37 °C. After incubation, the cells were washed with PBS and fresh glucose-free DMEM containing 100 μM 2NBDG added for 30 min. Then, cells were washed three times with ice-cold PBS to remove excess fluorescence in the wells, and fluorescence was measured using a microplate reader at excitation and emission wavelengths of 485 and 530 nm, respectively. Background was subtracted from all values. The cells were then lysed, the protein content was determined in each experiment with a BCA protein assay kit. For each experiment, at least two assays of each condition were performed, and each experiment was repeated at least three times.^[55]

Phosphorylation of PTP1B substrates. It was analysed by western blot.^[56] Antibodies were purchased from Cell Signaling Technology Inc. In brief, cell lysates were subjected to 5 or 12% SDS-PAGE. Proteins were transferred to a polyvinylidene difluoride membrane. The membranes were then blocked for 1 hour at room temperature with 3% BSA in Tris-buffered saline containing 0.1% Tween 20. Immunostaining to detect each protein was achieved with O/N incubation with a 1:1,000 dilution of anti-phosphospecific anti-IRS, anti-AKT or anti-STAT3 antibodies. Membranes were also blotted

with anti-total anti-IRS, anti-AKT or anti-STAT3 antibodies. Specific total or phosphoproteins were visualized after subsequent incubation with a 1:5,000 dilution of anti-mouse or rabbit IgG conjugated to horseradish peroxidase and a SuperSignal Chemiluminescence detection procedure and imaged using an ImageQuant LAS 500 chemiluminescent detection chamber (General Electric Healthcare, Little Chalfont, UK). Densitometry was determined using ImageJ software (NIH). Three independent experiments were performed for each condition.

Molecular Modelling

Homology model of the holo structure of PTP1B was built using SWISS-MODEL web server, using as template the crystal structure of 1T48.^[46] QMEAN value resulted in -0.09 .^[57] Using the Protein Preparation Wizard module of the Schrödinger Suite (<http://www.Schrodinger.com>) the receptor geometry was optimized. The protonation states of charged amino acids were calculated with the PROPKA module.

The described ligands were built with the LigPrep module of Maestro, generating all possible states at $\text{pH } 7 \pm 2$, resulting in no protonated states for this series.

Docking experiments were performed using extra precision (XP) mode of the GLIDE module and a van der Waals radii scale factor of 1.0/0.8. Receptor grid was calculated using compound BB3 from 1T48 as the centre of the 10 Å-size box that enclosed the cryptic pocket. The lowest energy ligand poses were selected for further visual inspection and analysis of the ligand-receptor interactions.

Geometry optimization and charge distribution for each compound was obtained by the quantum mechanically calculated (RHF/3-21G**//RHF/6-31G**) as implemented in Gaussian 03 (Gaussian, Inc., Wallingford, CT).^[58]

MD simulations for each complex in the lowest energy docking pose were carried out with the general AMBER14 (<http://amberd.org/>) force field and the GAFF force field for the parametrization of the small molecules, using the same conditions as described previously.^[59] Systems were introduced in a truncated octahedron box of approximately 4000 TIP3P water molecules with 13 Å cut-off distance and sodium cations were added to achieve electrical neutrality. Smooth particle mesh Ewald (PME) method with a spacing grid of 1 Å was used for treating electrostatic interactions and SHAKE algorithm was applied to all hydrogen bonds with 2.0 fs integration step.^[60,61] An initial energy minimization of the water molecules and counter-ions was carried out on each system. The systems were further heated from 100 to 300 K in 25 ps, and solvent molecules were progressively allowed to move freely. To explore the complex between ligand and macromolecule 10 ns MD simulations were carried out without any restraints, generating snapshots each 20 ps for further analysis. The trajectories were collected and the cpptraj module from AMBER14 was used to calculate the root mean square deviation (RMSD) of the atomic positions of the ligands and the most populated conformers.^[62] Reference values were taken from Pro188 to Ser201 for α 3-helix, from Ala264 to Met282 for α 6-helix and from Ser286 to Trp291 for α 7-helix. The MM-ISMMA program was used to calculate the total binding energies for each compound.^[63] All the physicochemical properties and ADME parameters were obtained from web server SWISS-ADME (<http://www.swissadme.ch/>) and pIC50 values from the web server tool (<http://www.sanjeevslab.org/tools.html>).^[64]

Acknowledgements

Authors thank the financial support provided by: Spanish Ministerio de Economía y Competitividad (CTQ2017-85263-R MINECO/FEDER UE to J.J.V., MINECO RTI2018-097609-B-C21 to F.M.); Instituto de Salud Carlos III and FEDER funds (RD16/0009/0015, RD16/0009/18, PI17/01513 and PI17/00625to J.J.V., D.R.-P. and M.R.-P.); Comunidad de Madrid (NOVELREN, B2017/BMD-3751 to J.J.V. and D.R.-P.); and Fundación Renal Íñigo Alvarez de Toledo (FRIAT). Fellowships were provided by: REDinREN and University of Alcalá (to P.S.-A. and J.G.-M.); Ministerio de Economía y Competitividad (FPU16/01647to J.G.-M); and Ministerio de Educación, Cultura y Deporte (FPU15/02857 to B.D.G.). We acknowledge BioSolvelt for a free one-year licence for FlexX software to J.G.-M (Scientific Challenge, Winter 2017) and to ChemAxon for a free three-year license for Marvin Suite software. We also thank Dr. Ryan Walsh (INRS, Québec, Canada) for his kind advice and comments.

Conflict of Interest

The authors declare no conflict of interest.

Keywords: biological activity · inhibitors · insulin mimetics · PTP1B · pyrrolo[1,2-*a*]quinoxaline

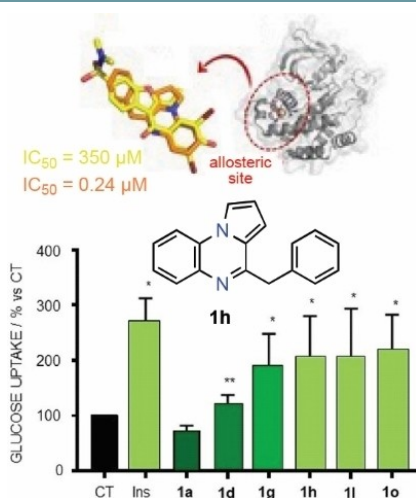
- [1] B. J. Goldstein, A. Bittner-Kowalczyk, M. F. White, M. Harbeck, *J. Biol. Chem.* **2000**, *275*, 4283–4289.
- [2] S. Dadke, J. Kusari, J. Chernoff, *J. Biol. Chem.* **2000**, *275*, 23642–23647.
- [3] M. Delibegovic, D. Zimmer, C. Kauffman, K. Rak, E. G. Hong, Y. R. Cho, J. K. Kim, B. B. Kahn, B. G. Neel, K. K. Bence, *Diabetes* **2009**, *58*, 590–599.
- [4] L. D. Klamon, O. Boss, O. D. Peroni, J. K. Kim, J. L. Martino, J. M. Zabolotny, N. Moghal, M. Lubkin, Y. B. Kim, A. H. Sharpe, A. Stricker-Krongrad, G. I. Shulman, B. G. Neel, B. B. Kahn, *Mol. Cell. Biol.* **2000**, *20*, 5479–5489.
- [5] M. Elchebly, P. Payette, E. Michaliszyn, W. Cromlish, S. Collins, A. L. Loy, D. Normandin, A. Cheng, J. Himms-Hagen, C. C. Chan, C. Ramachandran, M. J. Gresser, M. L. Tremblay, B. P. Kennedy, *Science* **1999**, *283*, 1544–1548.
- [6] C. M. Rondinone, J. M. Trevillyan, J. Clampit, R. J. Gum, C. Berg, P. Kroeger, L. Frost, B. A. Zinker, R. Reilly, R. Ulrich, M. Butler, B. P. Monia, M. R. Jirousek, J. F. Waring, *Diabetes* **2002**, *51*, 2405–2411.
- [7] B. A. Zinker, C. M. Rondinone, J. M. Trevillyan, R. J. Gum, J. E. Clampit, J. F. Waring, N. Xie, D. Wilcox, P. Jacobson, L. Frost, P. E. Kroeger, R. M. Reilly, S. Koterski, T. J. Oppenorth, R. G. Ulrich, S. Crosby, M. Butler, S. F. Murray, R. A. McKay, S. Bhanot, B. P. Monia, M. R. Jirousek, *Proc. Natl. Acad. Sci. USA* **2002**, *99*, 11357–11362.
- [8] Trodusquemine (MSI-1436) completed phase I for obesity and T2DM and currently is suspended at phase I for breast cancer trials (www.clinicaltrials.gov).
- [9] Z. Y. Zhang, S. Y. Lee, *Expert Opin. Invest. Drugs*, **2003**, *12*, 223–33.
- [10] K. A. Lantz, S. G. Hart, S. L. Planey, M. F. Roitman, I. A. Ruiz-White, H. R. Wolfe, M. P. McLane, *Obesity*, **2010**, *18*, 1516–1523.
- [11] S. Fukuda, T. Ohta, S. Sakata, H. Morinaga, M. Ito, Y. Nakagawa, M. Tanaka, M. Matsushita, *Diabetes Obes. Metab.* **2010**, *12*, 299–306.
- [12] E. J. Moran, S. Sarshar, J. F. Cargill, M. M. Shahbaz, A. Lio, A. M. M. Mjalli, R. W. Armstrong, *J. Am. Chem. Soc.* **1995**, *117*, 10787–10788.
- [13] L.-J. Wang, B. Jiang, N. Wu, S.-Y. Wang, D.-Y. Shi, *RSC Adv.* **2015**, *5*, 48822–48834.
- [14] A. P. Combs, *J. Med. Chem.* **2010**, *53*, 2333–2344.
- [15] S. De Munter, M. Kohn, M. Bollen, *ACS Chem. Biol.* **2013**, *8*, 36–45.
- [16] W. Peti, R. Page, *Bioorg. Med. Chem.* **2015**, *23*, 2781–2785.
- [17] M. A. Ghattas, N. Raslan, A. Sadeq, M. Al Sorkhy, N. Atatreh, *Drug Des. Dev. Ther.* **2016**, *10*, 3197–3209.
- [18] D. Barford, A. J. Flint, N. K. Tonks, *Science* **1994**, *263*, 1397–1404.
- [19] A. Salmeen, J. N. Andersen, M. P. Myers, N. K. Tonks, D. Barford, *Mol. Cell* **2000**, *6*, 1401–1412.
- [20] Y. A. Puius, Y. Zhao, M. Sullivan, D. S. Lawrence, S. C. Almo, Z.-Y. Zhang, *Proc. Natl. Acad. Sci. USA* **1997**, *94*, 13420–13425.
- [21] P. J. Ala, L. Gonneville, M. Hillman, M. Becker-Pasha, E. W. Yue, B. Douthy, B. Wayland, P. Polam, M. L. Crawley, E. McLaughlin, R. B. Sparks, B. Glass, A. Takvorian, A. P. Combs, T. C. Burn, G. F. Hollis, R. Wynn, *J. Biol. Chem.* **2006**, *281*, 38013–38021.
- [22] C. Wiesmann, K. J. Barr, J. Kung, J. Zhu, D. A. Erlanson, W. Shen, B. J. Fahr, M. Zhong, L. Taylor, M. Randal, R. S. McDowell, S. K. Hansen, *Nat. Struct. Mol. Biol.* **2004**, *11*, 730–737.
- [23] N. Krishnan, D. Koveal, D. H. Miller, B. Xue, S. D. Akshinthala, J. Kragelj, M. R. Jensen, C.-M. Gauss, R. Page, M. Blackledge, S. K. Muthuswamy, W. Peti, N. K. Tonks, *Nat. Chem. Biol.* **2014**, *10*, 558–566.
- [24] A. Huang, A. Ma, *Mini-Rev. Med. Chem.* **2013**, *13*, 607–616.
- [25] G. W. H. Cheeseman, B. Tuck, *J. Chem. Soc.* **1966**, 852–855.
- [26] M. L. Heffernan, G. M. Irvine, *Aust. J. Chem.* **1976**, 837–845.
- [27] J. Montalibet, K. I. Skorey, B. P. Kenedy, *Methods* **2005**, *23*, 2–8.
- [28] J. García-Marín, *J. Biomol. Struct. Dyn.* **2020**. DOI: 10.1080/07391102.2020.1790421.
- [29] R. A. Walsh, *PeerJ* **2018**, *6*, e6082.
- [30] R. A. Walsh, *Anal. Biochem.* **2019**, *572*, 58–62.
- [31] J. J. Irwin, D. Duan, H. Torosyan, A. K. Doak, K. T. Ziebart, T. Sterling, G. Tumanian, B. K. Shoichet, *J. Med. Chem.* **2015**, *58*, 7076–7087.
- [32] S. L. McGovern, E. Caselli, N. Grigorieff, B. K. Shoichet, *J. Med. Chem.* **2002**, *45*, 1712–1722.
- [33] S. Boulton, R. Selvaratnam, R. Ahmed, K. Van, X. Cheng, G. Melacini, *J. Med. Chem.* **2019**, *62*, 5063–5079.
- [34] D. Duan, H. Torosyan, D. Elnatan, C. K. McLaughlin, J. Logie, M. S. Shoichet, D. A. Agard, B. K. Shoichet, *ACS Chem. Biol.* **2017**, *12*, 282–290.
- [35] H. Torosyan, B. K. Shoichet, *J. Med. Chem.* **2019**, *62*, 9593–9599.
- [36] A. N. Ganesh, E. N. Donders, B. K. Shoichet, M. S. Shoichet, *Nano Today*, **2018**, *19*, 188–200.
- [37] P. Lewi, E. Arnold, K. Andries, H. Bohets, H. Borghys, A. Clark, F. Daeyaert, K. Das, M. P. de Bethune, M. de Jonge, J. Heeres, L. Koymans, J. Leempoels, J. Peeters, P. Timmerman, W. Van den Broeck, F. Vanhoutte, G. Van't Klooster, M. Vinkers, Y. Volovik, P. A. Janssen, *Drugs R&D*, **2004**, *5*, 245–257.
- [38] S. R. LaPlante, R. Carson, J. Gillard, N. Aubry, R. Coulombe, S. Bordeleau, P. Bonneau, M. Little, J. O'Meara, P. L. Beaulieu, *J. Med. Chem.* **2013**, *56*, 5142–5150.
- [39] J. M. Lopez-Nicolas, M. Perez-Gilbert, F. Garcia-Carmona, *J. Agric. Food Chem.* **2009**, *57*, 4630–4635.
- [40] M. F. Sassano, A. K. Doak, B. L. Roth, B. K. Shoichet, *J. Med. Chem.* **2013**, *56*, 2406–2414.
- [41] D. Duan, A. K. Doak, L. Nedyalkova, B. K. Shoichet, *ACS Chem. Biol.* **2015**, *10*, 978–988.
- [42] H. M. Berman, J. Westbrook, Z. Feng, G. Gilliland, T. N. Bhat, H. Weissig, I. N. Shindyalov, P. E. Bourne, *Nucleic Acids Res.* **2000**, *28*, 235–242.
- [43] A. J. Barr, *Future Med. Chem.* **2010**, *2*, 1563–1576.
- [44] FlexX version 4.0; BioSolvelt GmbH, Sankt Augustin, Germany, **2019**, www.biosolvelt.de/FlexX.
- [45] S. Li, J. Zhang, S. Lu, W. Huang, L. Geng, Q. Shen, J. Zhang, *PLoS One* **2014**, *9*, e97668/1–e97668/10.
- [46] L. Bordoli, F. Kiefer, K. Arnold, P. L. Benkert, J. Battey, T. Schwede, *Nat. Protoc.* **2009**, *4*, 1–13.
- [47] W. Cui, Y.-H. Cheng, L.-L. Geng, D.-S. Liang, T.-J. Hou, M.-J. Ji, *J. Chem. Inf. Model.* **2013**, *53*, 1157–1167.
- [48] A. Daina, O. Michielin, V. Zoete, *Sci. Rep.* **2017**, *7*, 42717/1–42717/13.
- [49] J. Baell, M. A. Walters, *Nature* **2014**, *513*, 481–483.
- [50] A. Daina, O. Michielin, V. Zoete, *J. Chem. Inf. Model.* **2014**, *54*, 3284–3301.
- [51] C. Abad-Zapatero, J. T. Metz, *Drug Discovery Today* **2005**, *10*, 464–469.
- [52] H. Yuan, Y. Hu, Y. Zhu, Y. Zhang, C. Luo, Z. Li, T. Wen, W. Zhuang, J. Zou, L. Hong, X. Zhang, I. Hisatome, T. Yamamoto, J. Cheng, *Mol. Cell. Endocrinol.* **2017**, *443*, 138–145.
- [53] F. Angius, A. Floris, *Toxicol. in Vitro* **2015**, *29*, 314–319.
- [54] H. Yoshitomi, R. Tsuru, L. Li, J. Zhou, M. Kudo, T. Liu, M. Gao, *PLoS One*, **2017**, *8*, e0183988/1–e0183988/13.
- [55] M. Hatem-Vaquero, M. Griera, A. García-Jerez, A. Luengo, J. Álvarez, J. A. Rubio, L. Calleros, D. Rodríguez-Puyol, M. Rodríguez-Puyol, S. De Frutos, *J. Endocrinol.* **2017**, *234*, 115–128.
- [56] N. Guex, M. C. Peitsch, T. Schwede, *Electrophoresis*, **2009**, *30*, S162–S173.

- [57] P. Benkert, M. Kuenzli, T. Schwede, *Nucleic Acids Res.* **2009**, *37*, W510–W514.
- [58] M. J. Frisch, G. W. Trucks, H. B. Schlegel, G. E. Scuseria, M. A. Robb, J. R. Cheeseman, J. A. Montgomery, Jr., T. Vreven, K. N. Kudin, J. C. Burant, J. M. Millam, S. S. Iyengar, J. Tomasi et al., *Gaussian 03, Revision C.02*, Gaussian, Inc.: Wallingford CT, **2004**.
- [59] M. Purwn, J. Hernandez-Toribio, C. Coderch, R. Panchuk, N. Skorokhyd, K. Filipiak, B. de Pascual-Teresa, A. Ramos, *RSC Adv.* **2016**, *6*, 66595–66608.
- [60] T. Darden, D. York, L. Pedersen, *J. Chem. Phys.* **1993**, *92*, 10089–10092.
- [61] M. A. Lill, *Biochemistry*, **2011**, *50*, 6157–6169.
- [62] D. R. Roe, T. E. Cheatham, *J. Chem. Theory Comput.* **2013**, *9*, 3084–3095.
- [63] J. Klett, A. Nunez-Salgado, H. G. Dos Santos, A. Cortes-Cabrera, A. Perona, R. Gil-Redondo, D. Abia, F. Gago, A. Morreale, *J. Chem. Theory Comput.* **2012**, *8*, 3395–3408.
- [64] C. Selvaraj, S. K. Tripathi, K. K. Reddy, S. K. Singh, *Curr. Trends Biotechnol. Pharm.* **2011**, *5*, 1104–1109.

Manuscript received: June 20, 2020
Revised manuscript received: July 29, 2020
Version of record online: ■■■, ■■■■

FULL PAPERS

Rather picky: Pyrrolo[1,2-*a*]quinoxalines substituted at C1–C4 and C7–C8 behave as insulin mimetics that potently and selectively inhibit PTP1B rather than its closest homologue TCPTP. They bind to the $\alpha 3/\alpha 6/\alpha 7$ tunnel in MD simulations and form stable aggregates in equilibrium with aggregator in buffered solutions. The 4-benzyl derivative also inhibits p-AKT and p-IRS.



J. García-Marín, M. Giera, Dr. P. Sánchez-Alonso, B. Di Geronimo, Prof. F. Mendicuti, Prof. M. Rodríguez-Puyol, Dr. R. Alajarín*, Prof. B. de Pascual-Teresa, Prof. J. J. Vaquero*, Dr. D. Rodríguez-Puyol**

1 – 15

Pyrrolo[1,2-*a*]quinoxalines: Insulin Mimetics that Exhibit Potent and Selective Inhibition against Protein Tyrosine Phosphatase 1B

